

# Light Trapping for Solar Fuel Generation with Mie Resonances

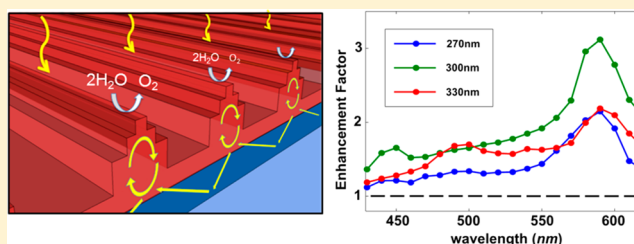
Soo Jin Kim, Isabell Thomann, Junghyun Park, Ju-Hyung Kang, Alok P. Vasudev, and Mark L. Brongersma\*

Geballe Laboratory for Advanced Materials, 476 Lomita Mall, Stanford, California 94305-4045, United States

**S** Supporting Information

**ABSTRACT:** The implementation of solar fuel generation as a clean, terawatt-scale energy source is critically dependent on the development of high-performance, inexpensive photocatalysts. Many candidate materials, including for example  $\alpha$ -Fe<sub>2</sub>O<sub>3</sub> (hematite), suffer from very poor charge transport with minority carrier diffusion lengths that are significantly shorter (nanometer scale) than the absorption depth of light (micrometer scale near the band edge). As a result, most of the photoexcited carriers recombine rather than participate in water-splitting reactions. For this reason, there is a tremendous opportunity for photon management. Plasmon-resonant nanostructures have been employed to effectively enhance light absorption in the near-surface region of photocatalysts, but this approach suffers from intrinsic optical losses in the metal. Here, we circumvent this issue by driving optical resonances in the active photocatalyst material itself. We illustrate that judiciously nanopatterned photocatalysts support optical Mie and guided resonances capable of substantially enhancing the photocarrier generation rate within 10–20 nm from the water/photocatalyst interface.

**KEYWORDS:** Light trapping, Mie resonance, water splitting, solar fuel generation, iron oxide, photoelectrochemistry



Hydrogen generation by means of photoelectrochemical water splitting is capable of effectively converting solar energy into chemical energy, which can be stored and used when desired.<sup>1,2</sup> Significant time and resources have been expended on the development of the ideal, photocatalyst material. This material should not only be inexpensive and earth-abundant; it also needs to feature desirable light absorption and charge transport properties, a favorable electronic bandstructure, and a high catalytic activity. No single material currently combines all of these challenging requirements. Several excellent candidate materials suffer from a large mismatch between the relevant electronic and photonic length scales, as very short carrier diffusion lengths (as short as ~10 nm) can prevent efficient collection of photogenerated carriers about an absorption depth (~0.1–10  $\mu$ m) away from the catalyst/liquid interface. Many activities have tried to overcome this challenge by either shortening the distance carriers need to travel or by enhancing the light absorption in the near-surface region. Examples of the first line of research include the use of porous and nanowire structures<sup>3–9</sup> with a large surface-to-volume ratio that make it easy for carriers to reach the surface. Examples for the second approach include the use of plasmonic particles<sup>10–16</sup> and Fabry–Perot resonances.<sup>10,17</sup> Whereas metallic nanostructures facilitate the most extreme light concentration, the use of metals for this purpose comes with undesirable optical losses. One way to get around this issue is to capitalize on the effective light absorption in metallic nanostructures to produce energetic, hot electrons capable of driving water splitting reactions.<sup>18</sup> Here, we propose an alternative pathway that circumvents such losses while

maintaining effective light concentration. This is accomplished by nanofashioning high-index photocatalyst materials into nanobeam-arrays that support strong optical resonances. By driving light concentrating resonances in the photocatalyst materials themselves rather than in metallic structures, light concentration and light absorption in photocatalyst materials can go hand-in-hand.

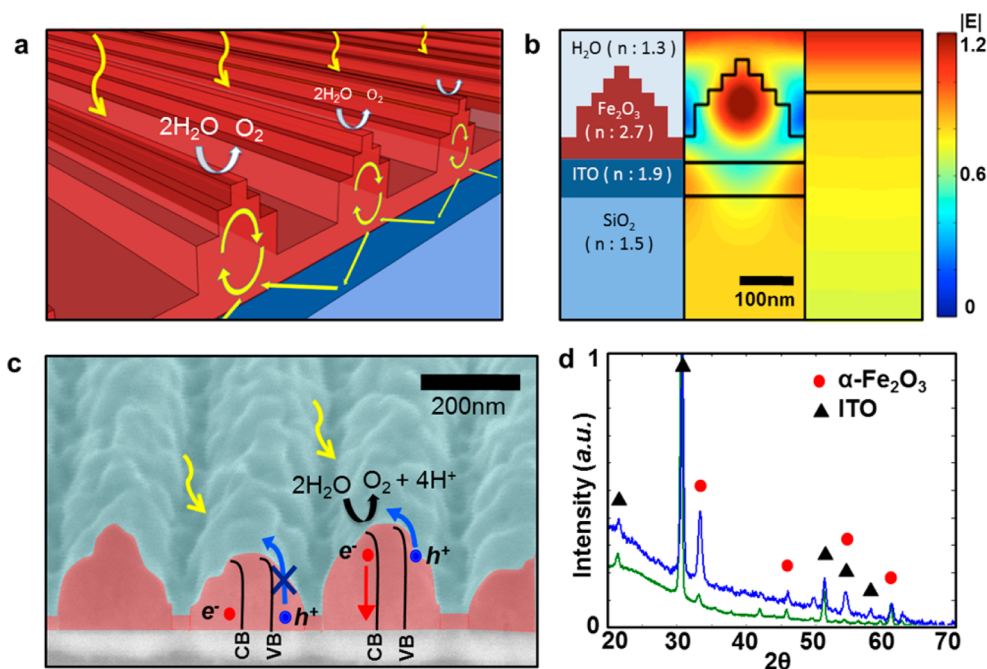
The proposed strategy capitalizes on the fact that deep subwavelength semiconductor nanostructures exhibit strong, leaky-mode optical resonances, just like their metallic counterparts.<sup>19–22</sup> In such small structures, resonances result from the ease with which high-index semiconductors are polarized by the electric field of the incident light. When a resonance is excited by sunlight both light absorption and light scattering can be enhanced.<sup>23,24</sup> By engineering the size, shape, spacing, and dielectric environment of the nanostructures the resonant wavelengths can be tuned across the solar spectrum. These desirable properties have demonstrated their benefits in a number of applications including photodetectors, nanostructured films with structural color, light localization, directional and magnetic antennas, and solar cells.<sup>25–32</sup>

Figure 1a schematically shows our proposed nanostructured photoelectrode consisting of an array of hematite nanobeams placed on top of an indium–tin oxide (ITO) coated glass substrate. When properly designed, the incident sunlight will

**Received:** December 10, 2013

**Revised:** February 6, 2014

**Published:** February 13, 2014



**Figure 1.** Overview of the proposed photon management strategy capable of enhancing water splitting rates with high-index photoelectrode materials. (a) Schematic view of hematite ( $\alpha\text{-Fe}_2\text{O}_3$ ) photoelectrode consisting of a periodic nanobeam-array (brown) on a conductive ITO layer (dark blue) that supports localized Mie and waveguide coupling resonances that boost the absorption of sunlight at the  $\text{Fe}_2\text{O}_3/\text{H}_2\text{O}$  interface. (b) Refractive index (left) and simulated electric field distributions for an optimized nanobeam electrode (center) and a planar, semi-infinite  $\text{Fe}_2\text{O}_3$  reference electrode (right) for an illumination wavelength of 590 nm. (c) Cross-sectional SEM images of a fabricated nanobeam photoanode, overlapped with schematic band diagrams that illustrate the photoexcitation of carriers, their transport, and the photoelectrochemical reactions they can drive when generated close to the  $\text{Fe}_2\text{O}_3/\text{H}_2\text{O}$  interface. (d) X-ray diffraction spectra taken from the hematite thin film with different grazing incident angles ( $\Omega$ ) for the X-rays. (green:  $2.5^\circ$ , blue:  $0.2^\circ$ ).

effectively couple to the localized leaky-mode optical resonances supported by the nanobeams, induce light absorption, and partially rescatter into the guided-mode resonances supported by the high-index  $\alpha\text{-Fe}_2\text{O}_3$  ( $n = 2.7$ ) and ITO ( $n = 1.9$ ) layers. It is important to emphasize that these two resonances have a distinct physical origin and thus can be engineered by manipulating different geometrical parameters. The localized leaky-mode resonances of the individual nanobeam are largely controlled by the nanobeam size and shape. The guided-mode resonances can be controlled either by manipulating the optical properties and thicknesses of the high-index waveguiding layers or by the nanobeam spacing, which governs the ability to grating-couple to the guided-mode resonances.

For application of nanobeams and wires in solar energy harvesting, it is worth noting that their optical resonances are broadband (quality factors  $Q$  are typically lower than 10) and occur for light polarized both along and orthogonal to the beam. Mie theory offers a framework to classify the different optical resonances supported by one-dimensional nanostructures<sup>21</sup> in terms of their polarization direction and azimuthal phase  $\varphi$  dependence of the scattered fields ( $\sim e^{im\varphi}$  where  $m$  is an integer that indicates the order of the resonance). Following this classification, the resonances with the electric field transverse to a nanobeam will be termed transverse electric (TE), and electric fields along the nanobeam will be termed transverse magnetic (TM). In this work, we analyze which resonant modes are most effective at enhancing solar fuel generation. It will be shown that the requirement to concentrate light extremely close to the water/photocatalyst interface makes the photon management strategy for solar fuel

generation somewhat more sophisticated than for thin-film solar cells; not only does the light need to be trapped in the photocatalyst, its spatial distribution needs to be controlled as well with deep-subwavelength precision.

We will illustrate the use of Mie resonances with iron oxide in the hematite phase, which serves as a prototypical high-index photoelectrode for water splitting.<sup>10,33–35</sup> Hematite is an earth-abundant, n-type semiconductor with a bandgap energy of about 2.1 eV (i.e., 590 nm)—a value considered close to optimal for water splitting by a single semiconductor material. It is chemically stable in an aqueous environment over a broad range of pH values and capable of absorbing photons across a relatively large portion of the solar spectrum, including most of the visible spectral range. In this aspect it outperforms other well-known catalyst materials such as  $\text{TiO}_2$  and  $\text{WO}_3$  that only absorb ultraviolet photons. Hematite's nemesis is its extremely short minority diffusion length of 2 nm.<sup>36,37</sup> This can be increased to 10–20 nm with the assistance of internal electric fields resulting from band bending at a semiconductor/liquid interface but remains very short compared to the absorption depth of light for most of the useful part of the solar spectrum.<sup>38</sup> This has severely hampered the development of this material as a photocatalyst viable for large-scale deployment. Photon management aimed at concentrating light very close to the semiconductor/liquid interface can hide this key weakness and make it more commercially interesting.<sup>39,40</sup>

Figure 1b demonstrates the benefits of an optimized nanobeam structure for water splitting. It shows how both the overall field intensity and the spatial distribution of the fields in the patterned photoelectrode material can be tailored

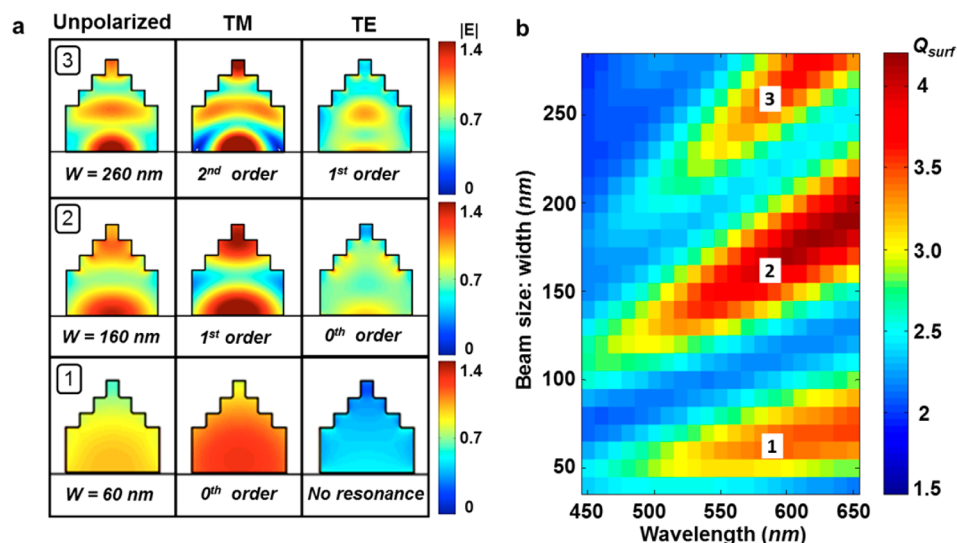


**Figure 2.** Optimization of the nanobeam size to maximize coupling to Mie resonances that enhance surface absorption. (a) Optical field profiles (electric field amplitude) for Mie resonances of different mode order as excited by unpolarized, transverse magnetic (TM) polarized or transverse electric (TE) polarized light. (b) Plot of the simulated surface absorption efficiency  $Q_{surf}$  versus nanobeam size and illumination wavelength. The magnitude of  $Q_{surf}$  quantifies how well a beam enhances light absorption near the  $\text{Fe}_2\text{O}_3/\text{H}_2\text{O}$  interface over a semi-infinite planar reference. This plot is calculated for unpolarized light.

to enhance light absorption near the  $\alpha\text{-Fe}_2\text{O}_3/\text{H}_2\text{O}$  interface as compared to a semi-infinite planar reference.

Figure 1c shows a scanning electron microscopy (SEM) image of one of the patterned nanobeam-arrays used in this study with a superimposed band diagram. The cross-sectional shape of each beam is qualitatively similar and approximated in our electromagnetic simulations. The band diagrams illustrate how optical excitation of an electron–hole pair will be followed by transport of holes toward the semiconductor/liquid interface where they can oxidize water to produce oxygen if carrier recombination of these minority carriers can be avoided. The photogenerated electrons are transported through the transparent oxide to an external circuit in which the generated photocurrent can be measured. In the absence of competing reactions, the magnitude of the photocurrent provides a direct measure of the rate of water splitting. In this work, we measure its spectral dependence and compare it to full-field electromagnetic simulations to verify that optical resonances can enhance this rate. The X-ray diffraction data presented in Figure 1d confirm the formation of the desired, chemically active hematite phase.

The most critical design parameter of the nanobeam-array is the nanobeam size. It determines which optical mode of the beams will be excited. This in turn governs the field distribution in the photoelectrode and thus where exactly the sunlight is absorbed in the structure. To illustrate this point, we start by analyzing the electric field distributions in individual hematite beams that result upon illumination with normally incident and TM polarized light at a wavelength of 590 nm. This wavelength is close to the bandgap of  $\text{Fe}_2\text{O}_3$ , where the intrinsic materials absorption is relatively weak. This wavelength is also close to the peak of the solar AM 1.5D spectrum, and for this reason the excitation of a resonance in this spectral location could provide significant benefits to the photocatalyst performance. Figure 2a shows the field distributions for beams with selected base widths of 60, 160, and 260 nm placed on a silica substrate. The 60 nm beam supports a zeroth-order ( $m = 0$ ) resonant TM mode in this spectral range and no TE mode. The larger 160

and 260 nm beams support higher-order modes for both TM and TE polarization. The higher-order resonances feature an increasing number of nodes in the field distribution along the vertical direction.

To analyze which beam size/resonant mode may be best for water splitting, we calculate an effective absorption cross section  $\sigma_{abs}$  defined as the absorbed power within a 20 nm region from the  $\text{H}_2\text{O}/\text{Fe}_2\text{O}_3$  interface divided by the power incident on the nanowire. This quantity has the dimensions of an area, and the magnitude of  $\sigma_{abs,NB}$  quantifies how effective a beam concentrates light in the near-surface region from which carriers can effectively be collected without significant recombination. To evaluate whether a beam structure outperforms a planar surface, we also calculate an equivalent number  $\sigma_{abs,P}$  for a section of a semi-infinite planar reference with the same width as the nanobeam. The ratio  $\sigma_{abs,NB}/\sigma_{abs,P}$  provides a direct measure of how well a beam could perform in enhancing water splitting over the reference and is termed the surface absorption efficiency  $Q_{surf}$ . Figure 2b shows a color map of  $Q_{surf}$  for different beam widths in the range from 20 to 280 nm and for wavelengths in the range from 450 to 650 nm, that is, where photon management can give rise to valuable contributions to the photocurrent. To evaluate the performance under solar illumination, we generate this map for unpolarized light. The red and yellow regions in the map can be directly linked to optical resonances in the nanobeams capable of producing substantial absorption gains over planar structures. The largest enhancements are found within three bands associated with the three TM resonances and two degenerate TE resonances shown in Figure 2a. For each resonance the resonance wavelength more-or-less linearly scales with the beam size, as expected for weakly dispersive materials. This feature enables controlled spectral tuning of the resonances. These resonances occur in nanobeams of any cross-sectional shape, and the absorption enhancement maps for different beam-shapes look qualitatively very similar. Based on this particular map, a 160 nm beam width appears to be an excellent choice for enhancing light absorption in the red part of the spectrum near 590 nm.



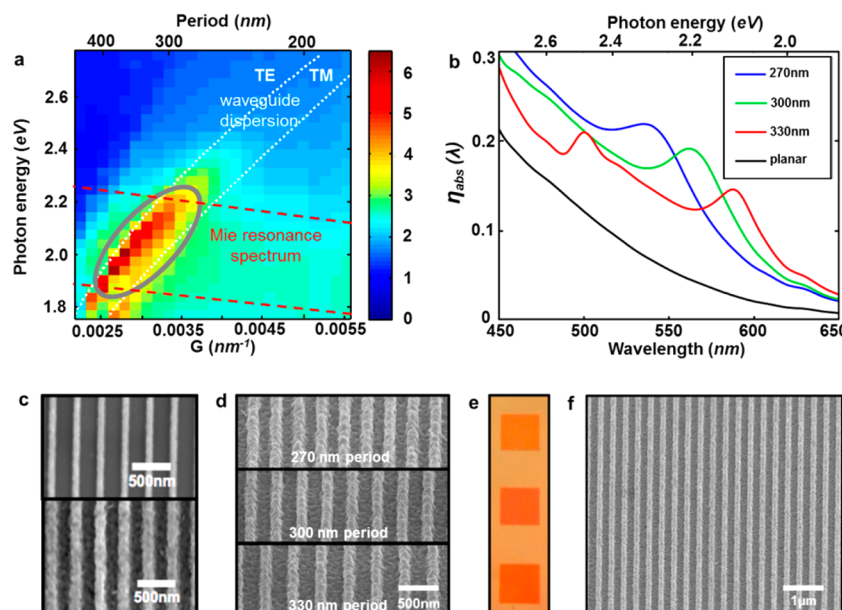


**Figure 3.** Joint optimization of guided and Mie resonances of the nanobeam array. (a) Enhancement factor for the surface absorption  $Q_{\text{surf}}$  with respect to the photon energy and reciprocal lattice vector of the nanobeam array. (b) Fraction of photons absorbed within 20 nm from the  $\text{Fe}_2\text{O}_3/\text{H}_2\text{O}$  interface for three different nanobeam array periods. (c) Top-view SEM image of an iron nanobeam-array before oxidation (top) and the  $\text{Fe}_2\text{O}_3$  nanobeam array produced upon oxidation (bottom). (d) SEM image of nanobeam-arrays with different periods. (e) Optical microscopy image of the nanobeam arrays shown in d. (f) Zoom-out SEM image showing the array uniformity over a larger sample area.

The first-order resonance produces the most favorable electric field distribution by placing one of its antinodes right at the beam/water interface. The zeroth-order mode features an unfavorably field distribution, a maximum in the core of the beam, and the second-order mode only shows one of its three antinodes at the surface. From this analysis, it is clear that the beam size is a critical design parameter. Whereas one might intuitively have predicted a linear scaling between the rate of water splitting and the active surface area, this should not be expected for the subwavelength structures considered here. In these subwavelength structures, only specific sizes support strong optical resonances and offer desirable spatial distributions of the electric field that can enhance the rate of water splitting. This can be seen from the vertical cross sections in Figure 2b that show an oscillation in  $Q_{\text{surf}}$  with increasing beam size.

Next, we optimize the spacing between the nanobeams to enable the most effective grating coupling to waveguide-mode resonances with beams of a fixed, optimum size of 160 nm. The nanobeams were placed on a 20-nm-thick, continuous hematite layer that prevents chemical interactions with the underlying ITO layer. This layer was chosen to be 50-nm-thick to allow for sufficient electrical conductivity and to enable the high-index hematite/ITO layer to support single TE and TM guided mode resonances. To optimize the grating coupling with nanobeams, we first calculate  $Q_{\text{surf}}$  for a range of photon energies  $E$  and array periods  $P$ . This quantity is then plotted in a two-dimensional map as functions of  $E$  and the reciprocal lattice vector,  $G = 2\pi/P$  (Figure 3a). In such a map the physical mechanisms that give rise to the absorption enhancement can easily be identified and thus facilitate a thoughtful optimization. The absorption enhancement due to the localized Mie resonance shows up as a weakly dispersive (i.e., almost horizontal) feature and is outlined by the dashed red lines. This is consistent with the notion that these localized Mie resonances are more-or-less an intrinsic property of the beams

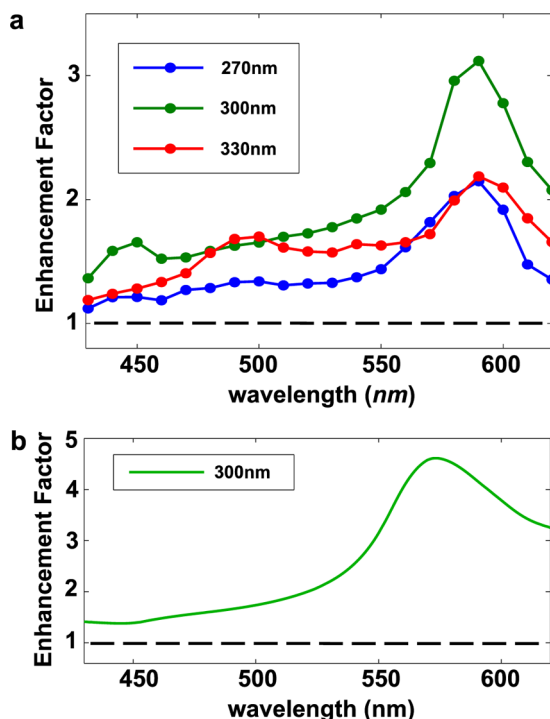
that is not greatly affected by the neighboring beams. The dispersive red feature in the map is related to the coupling to the TE and TM guided mode resonances. The optimal mode coupling conditions with respect to  $E$  and  $P$  were calculated by using the momentum matching condition ( $G = k$ ), where  $k = 2\pi n_{\text{eff}}/\lambda$  and  $n_{\text{eff}}$  is the effective mode-index for the quasi-guided mode supported by the nanobeam array. The mode coupling conditions for TE and TM modes are plotted as left and right white dashed lines in Figure 3a, respectively. It is noteworthy that the largest absorption enhancements are achieved in the region where the two enhancement mechanisms coincide. Here, localized Mie resonances in the beams can help in effectively redirecting light into the waveguided modes. Under such conditions, the optimum absorption enhancements of approximately a factor of 6 at 2.1 eV are obtained.

Figure 3b shows the absorption efficiency  $\eta_{\text{abs}}(\lambda)$ , defined as the fraction of solar photons absorbed within the first 20 nm from the  $\text{H}_2\text{O}$  surface. It can be seen that the absorption peak red-shifts and changes its magnitude with increasing  $P$ . For the period of around 300 nm, the absorption efficiency  $\eta_{\text{abs}}(\lambda)$  reaches approximately 20% in the spectral region near the band edge, whereas the planar reference absorbs less than 5%. It is clear that both the nanobeam size and the array period allow for a convenient spectral tuning of the absorption enhancement to maximize the overall solar absorption. To identify the optimum period, we calculate the predicted photocurrent density under AM 1.5D solar irradiation from  $J_{\text{ph}} = q \int \eta_{\text{abs}}(\lambda) S(\lambda) d\lambda$ , where  $S(\lambda)$  is the number of photons per unit wavelength, unit area and unit time for AM 1.5D solar irradiation (Supporting Information). Such calculations show that a semi-infinite planar cell can generate 0.85  $\text{mA}/\text{cm}^2$ . It also shows a close-to-optimum 300-nm-period nanobeam electrode can enhance this by 224% to 2.75  $\text{mA}/\text{cm}^2$ . Whereas larger periods are capable of producing larger peak enhancements (Supporting Information), it was found that the overall enhancement was in fact lower as these large enhancements are attained in the spectral

region close to the bandgap, where the material does not absorb strongly in absolute terms.

Samples with nanobeam arrays were fabricated to experimentally demonstrate the enhanced performance of judiciously nanopatterned photoelectrodes (Figure 3c–f). This was accomplished in a multistep process, involving an initial lithographic step to define the Fe beams and a high temperature oxidation step to convert them into hematite beams. The increase in the beam size upon oxidation resulting from oxygen incorporation is shown in top-view SEM images (Figure 3c). Figure 3d show three SEM images of arrays with different array periods. The corresponding optical, white-light reflection images show the different optical appearance of these samples and provide a very direct way to observe the tunability of the optical properties with the period. Figure 3f is an overview image showing the uniformity of the beam size and spacing across a larger sample area.

Figure 4a shows the experimental photocurrent enhancement spectra for arrays with beam periods of 270, 300, and 330 nm.



**Figure 4.** Experimental and simulated photocurrent enhancement spectra for several nanobeam electrodes. (a) Experimental photocurrent enhancement spectra for nanobeam photoelectrodes with different nanobeam periods. The enhancement was measured with respect to a planar, unpatterned section of the same photoelectrode. All spectra show a peak in the spectral region between 550 and 600 nm that is attributed to a Mie resonance supported by nanobeams. The enhancement is largest when the period of the nanobeam array is chosen such that the guided resonance is at the same frequency as the Mie resonance ( $P = 300$  nm). (b) The simulated photocurrent enhancement spectrum for a nanobeam array with the optimized period of 300 nm.

These were obtained by first measuring the photocurrent obtained from an area of the photoelectrode with nanobeams and normalizing it to the photocurrent obtained from an unpatterned area. All of the experimental spectra show a clear enhancement peak in the spectral region ranging from 570 to 610 nm. The sample with the optimum 300-nm-period shows

the largest enhancement. Figure 4b shows the simulated photocurrent enhancement spectrum that was calculated for the nanobeam array with the optimum period of 300 nm. Its spectral properties are qualitatively similar to the experimental spectra with a broadband enhancement across the entire probed spectral range and a peak in the same spectral range. The absolute enhancement in the experiments was found to be lower than in the simulations. This can possibly be explained by the fact that the diffusion length of our samples is not as high as some of the ones quoted in the literature (and used in our simulations). Another possible origin may be a slight undulation in the beam size along its length. The peak in the spectra collocates with the predicted location of the optical Mie resonance of the nanobeams and the guided mode resonance. A more detailed, polarization-dependent analysis of the photocurrent enhancement shows that the TM polarization most significantly contributes to the overall enhancement due to a 2-fold degeneracy of this mode<sup>19</sup> (Supporting Information, Figure S5).

In this work, we have analyzed the beneficial effects of judiciously nanostructuring the iron oxide photoanode of a watersplitting device to overcome the detrimental mismatch between its electronic (carrier diffusion length) and photonic (absorption depth) length scales. Nanostructuring allows sunlight to drive optical resonances that can both enhance the light intensity inside the photoelectrode and favorably redistribute the highest fields to the near surface region. The important roles of the nanostructure size and arrangement on the surface were highlighted, and it was shown how these determine the spectral location and magnitude of the optical resonances. The importance of these resonances was verified experimentally using spectral photocurrent measurements. The presented procedure could be extended to cells with thicker waveguiding layers supporting multiple modes and two-dimensional arrangements of Mie scatterers. It can also guide the design of other large-area synthesis procedures for roughened photoelectrode materials by providing information on the desired amplitude and spatial frequencies of the surface roughness. As many popular photocatalyst materials are high-index semiconductors, the above procedures are quite general and even beneficial to semiconductors nanoelectrodes with larger carrier diffusion lengths. With the increased availability of chemical synthesis routes and nanopatterning techniques, it is likely that optimized nanostructure arrays will be realizable inexpensively and over large areas. As such, this work contributes to the development of future generations of high-performance photoelectrodes for solar fuel generation.

**Methods.** Fe nanobeams are defined lithographically over areas of 0.25 mm<sup>2</sup> and overcoated with a 10-nm-thick continuous Fe layer. The iron nanobeams are then transformed to iron oxide beams by calcination in air at 600 °C for 4–5 min. X-ray diffraction was used to confirm the presence of the hematite ( $\alpha$ -phase of iron oxide). Photocurrent measurements are performed with a three-electrode photoelectrochemical cell built into an optical microscope. A platinum mesh is used as the counter electrode, and Ag/AgCl is used as a reference electrode. Photocurrent is measured at the constant bias of 1.4 V vs reversible hydrogen electrode (RHE) under the illumination with light from a supercontinuum white light source (Fianium). The illumination wavelength was controlled using an acousto-optical tunable filter with bandwidth of 10 nm. The light was lightly focused on the sample area using  $\times 2$  microscope objective. Full-field electromagnetic simulations of

the light absorption are performed based on the finite difference frequency domain (FDFD) technique. The absorbed power in a certain volume of interest in the nanobeams is calculated from the Ohmic loss of  $\text{Fe}_2\text{O}_3$ , that is,  $\int \omega \cdot \text{Im}(\epsilon) |\mathbf{E}|^2 dV$ , where  $\epsilon$  is the complex dielectric constant of  $\text{Fe}_2\text{O}_3$ .

## ■ ASSOCIATED CONTENT

### ● Supporting Information

Supplementary methods and figures depicting the simulated absorption enhancement factor for nanobeams for TE and TM polarization and also for nanobeam arrays, vertical cross-sections of Figure 2a and AM1.5D integrated photocurrent generation, fabrication steps for the nanobeam photoanodes, photocurrent measurement and experimental setup, and experimental photocurrent enhancement spectra with SEM images of the measured nanobeam structure. This material is available free of charge via the Internet at <http://pubs.acs.org>.

## ■ AUTHOR INFORMATION

### Corresponding Author

\*E-mail: [brongersma@stanford.edu](mailto:brongersma@stanford.edu).

### Present Address

I.T.: Department of Electrical and Computer Engineering, Rice University, 6100 Main St. - MS 378, Houston, Texas 77005-1892, United States.

### Notes

The authors declare no competing financial interest.

## ■ ACKNOWLEDGMENTS

We greatly acknowledge support from Samsung and the Center on Nanostructuring for Efficient Energy Conversion (CNEEC), an Energy Frontier Research Center funded by the U.S. Department of Energy, Office of Science, Basic Energy Sciences under Award DE-SC0001060 and DOE grant DE-FG02-07ER46426.

## ■ REFERENCES

- (1) Walter, M. G.; Warren, E. L.; McKone, J. R.; Boettcher, S. W.; Mi, Q.; Santori, E. A.; Lewis, N. S. Solar Water Splitting Cells. *Chem. Rev.* **2010**, *110*, 6446.
- (2) Fujishima, A.; Honda, K. Electrochemical Photolysis of Water at a Semiconductor Electrode. *Nature* **1972**, *238*, 37.
- (3) Kay, A.; Cesar, I.; Grätzel, M. New Benchmark for Water Photooxidation by Nanostructured  $\alpha\text{-Fe}_2\text{O}_3$  Films. *J. Am. Chem. Soc.* **2006**, *129*, 15714.
- (4) Cesar, I.; Sivula, K.; Kay, A.; Zboril, R.; Grätzel, M. Influence of Feature Size, Film Thickness, and Silicon Doping on the Performance of Nanostructured Hematite Photoanodes for Solar Water Splitting. *J. Phys. Chem. C* **2009**, *113*, 772.
- (5) Ling, Y.; Wang, G.; Wheeler, D. A.; Zhang, J. Z.; Li, Y. Sn-Doped Hematite Nanostructures for Photoelectrochemical Water Splitting. *Nano Lett.* **2011**, *11*, 2119.
- (6) Boettcher, S. W.; Spurgeon, J. M.; Putnam, M. C.; Warren, E. L.; Turner-Evans, D. B.; Kelzenberg, M. D.; Maiolo, J. R.; Atwater, H. A.; Lewis, N. S. Energy-Conversion Properties of Vapor-Liquid-Solid-Grown Silicon Wire-Array Photocathodes. *Science* **2010**, *327*, 185.
- (7) Goodey, A. P.; Eichfeld, S. M.; Lew, K.-K.; Redwing, J. M.; Mallouk, T. E. Silicon Nanowire Array Photoelectrochemical Cells. *J. Am. Chem. Soc.* **2007**, *129*, 12344.
- (8) Beermann, N.; Vayssieres, L.; Lindquist, S.-E.; Hagfeldt, A. Photoelectrochemical Studies of Oriented Nanorod Thin Films of Hematite. *J. Electrochem. Soc.* **2000**, *147*, 2456.
- (9) Lin, Y.; Zhou, S.; Sheehan, S. W.; Wang, D. Nanonet-Based Hematite Heteronanostructures for Efficient Solar Water Splitting. *J. Am. Chem. Soc.* **2011**, *133*, 2398.
- (10) Thomann, I.; Pinaud, B. A.; Chen, Z.; Clemens, B. M.; Jaramillo, T. F.; Brongersma, M. L. Plasmon Enhanced Solar-to-Fuel Energy Conversion. *Nano Lett.* **2011**, *11*, 3440.
- (11) Gao, H.; Liu, C.; Jeong, H. E.; Yang, P. Plasmon-Enhanced Photocatalytic Activity of Iron Oxide on Gold Nanopillars. *ACS Nano* **2012**, *6*, 234.
- (12) Lee, J.; Mubeen, S.; Ji, X.; Stucky, G. D.; Moskovits, M. Plasmonic Photoanodes for Solar Water Splitting with Visible Light. *Nano Lett.* **2012**, *12*, 5014.
- (13) Chen, J.-J.; Wu, J. C. S.; Wu, P. C.; Tsai, D. P. Improved Photocatalytic Activity of Shell-Isolated Plasmonic Photocatalyst  $\text{Au@SiO}_2/\text{TiO}_2$  by Promoted LSPR. *J. Phys. Chem. C* **2012**, *116*, 26535.
- (14) Linic, S.; Christopher, P.; Ingra, D. B. Plasmonic-metal nanostructures for efficient conversion of solar to chemical energy. *Nat. Mater.* **2011**, *10*, 911.
- (15) Warren, S. C.; Thimsen, E. Plasmonic solar water splitting. *Energy Environ. Sci.* **2012**, *5*, 5133.
- (16) Thimsen, E.; Formal, F. L.; Grätzel, M.; Warren, S. C. Influence of Plasmonic Au Nanoparticles on the Photoactivity of  $\text{Fe}_2\text{O}_3$  Electrodes for Water Splitting. *Nano Lett.* **2011**, *11*, 35.
- (17) Dotan, H.; Kfir, O.; Sharlin, E.; Blank, O.; Gross, M.; Dumchin, I.; Ankonina, G.; Rothschild, A. Resonant light trapping in ultrathin films for water splitting. *Nat. Mater.* **2013**, *12*, 158–164.
- (18) Mubeen, S.; Lee, J.; Singh, N.; Krämer, S.; Stucky, G. D.; Moskovits, M. An autonomous photosynthetic device in which all charge carriers derive from surface plasmons. *Nat. Nanotechnol.* **2013**, *8*, 247.
- (19) Cao, L.; White, J. S.; Park, J.-S.; Schuller, J. A.; Clemens, B. M.; Brongersma, M. L. Engineering light absorption in semiconductor nanowire devices. *Nat. Mater.* **2009**, *8*, 643.
- (20) Muskens, O. L.; Diedenhofen, S. L.; Kaas, B. C.; Algra, R. E.; Bakkers, E. P. A. M.; Rivas, J. G.; Lagendijk, A. Large Photonic Strength of Highly Tunable Resonant Nanowire Materials. *Nano Lett.* **2009**, *9*, 930.
- (21) Bohren, C. F.; Huffman, D. R. *Absorption and Scattering of Light by Small Particles*; Wiley: New York, 1998.
- (22) Maier, S. A.; Atwater, H. A. Plasmonics: Localization and guiding of electromagnetic energy in metal/dielectric structures. *J. Appl. Phys.* **2005**, *98*, 011101.
- (23) Luk'yanchuk, B. S.; Miroshnichenko, A. E.; Tribelsky, M. I.; Kivshar, Y. S.; Khokhlov, A. R. Paradoxes in laser heating of plasmonic nanoparticles. *New J. Phys.* **2012**, *14*, 093022.
- (24) Shi, L.; Harris, J. T.; Fenollosa, R.; Rodriguez, I.; Lu, X.; Korgel, B. A.; Meseguer, F. Monodisperse silicon nanocavities and photonic crystals with magnetic response in the optical region. *Nat. Commun.* **2013**, *4*, 1904.
- (25) Cao, L.; Fan, P.; Barnard, E. S.; Brown, A. M.; Brongersma, M. L. Tuning the color of silicon nanostructures. *Nano Lett.* **2010**, *10*, 2649.
- (26) Muskens, O. L.; Diedenhofen, S. L.; Kass, B. C.; Algra, R. E.; Bakkers, E. P. A. M.; Rivas, J. G.; Lagendijk, A. Large Photonic Strength of Highly Resonant Nanowire Materials. *Nano Lett.* **2009**, *9*, 930.
- (27) Cao, L.; Fan, P.; Vasudev, A. P.; White, J. S.; Yu, Z.; Cai, W.; Schuller, J. A.; Fan, S.; Brongersma, M. L. Semiconductor Nanowire Optical Antenna Solar Absorbers. *Nano Lett.* **2010**, *10*, 439.
- (28) Granddier, J.; Callahan, D. M.; Munday, J. N.; Atwater, H. A. Light Absorption Enhancement in Thin-Film Solar Cells Using Whispering Gallery Modes in Dielectric Nanospheres. *Adv. Mater.* **2011**, *23*, 1272.
- (29) Spinelli, P.; Verschuuren, M. A.; Polman, A. Broadband omnidirectional antireflection coating based on subwavelength surface Mie resonators. *Nat. Commun.* **2012**, *3*, 692.
- (30) Yu, Y.; Ferry, V. E.; Alivisatos, A. P.; Cao, L. Dielectric Core-Shell Optical Antennas for Strong Solar Absorption Enhancement. *Nano Lett.* **2012**, *12*, 3674.
- (31) Cao, L.; Park, J.-S.; Fan, P.; Clemens, B.; Brongersma, M. L. Resonant Germanium Nanoantenna Photodetectors. *Nano Lett.* **2010**, *10*, 1229.

- (32) Person, S.; Jain, M.; Saenz, J. J.; Wicks, G.; Novotny, L. Demonstration of zero optical backscattering from single nanoparticles. *Nano Lett.* **2013**, *13*, 1806.
- (33) Sivula, K.; Formal, F. L.; Grätzel, M. Solar Water Splitting: Progress Using Hematite ( $\alpha$ -Fe<sub>2</sub>O<sub>3</sub>) Photoelectrodes. *ChemSusChem* **2011**, *4*, 432.
- (34) Katza, M. J.; Riha, S. C.; Jeong, N. C.; Martinson, A. B. F.; Farha, O. K.; Hupp, J. T. Toward solar fuels: Water splitting with sunlight and “rust”? *Coord. Chem. Rev.* **2012**, *256*, 2521.
- (35) Wheeler, D. A.; Wang, G.; Ling, Y.; Li, Y.; Zhang, J. Z. Nanostructured hematite: synthesis, characterization, charge carrier dynamics, and photoelectrochemical properties. *Energy Environ. Sci.* **2012**, *5*, 6682.
- (36) Dotan, H.; Sivula, K.; Grätzel, M.; Rothschild, A.; Warren, S. C. Probing the photoelectrochemical properties of hematite ( $\alpha$ -Fe<sub>2</sub>O<sub>3</sub>) electrodes using hydrogen peroxide as a hole scavenger. *Energy Environ. Sci.* **2011**, *4*, 958.
- (37) Kennedy, J. H.; Frese, K. W., Jr. Photooxidation of Water at  $\alpha$ -Fe<sub>2</sub>O<sub>3</sub> Electrodes. *J. Electrochem. Soc.* **1978**, *125*, 709.
- (38) Dare-Edwards, M. P.; Goodenough, J. B.; Hamnett, A.; Trevellick, P. R. Electrochemistry and Photoelectrochemistry of Iron(III) Oxide. *J. Chem. Soc., Faraday Trans. I* **1983**, *79*, 2027.
- (39) Chen, Z.; Jaramillo, T. F.; Deutsch, T. G.; Kleiman-Shwarscstein, A.; Forman, A. J.; Gaillard, N.; Garland, R.; Takanabe, K.; Heske, C.; Sunkara, M.; McFarland, E. W.; Domen, K.; Miller, E. L.; Turner, J. A.; Dinh, H. N. Accelerating materials development for photoelectrochemical hydrogen production: Standards for methods, definitions, and reporting protocol. *J. Mater. Res.* **2010**, *25*, 3.
- (40) Bolton, J. R.; Strickler, S. J.; Connolly, J. S. Limiting and realizable efficiencies of solar photolysis of water. *Nature* **1985**, *316*, 495.